Biosensors and Bioelectronics 142 (2019) 111545

Contents lists available at ScienceDirect

Biosensors and Bioelectronics

journal homepage: www.elsevier.com/locate/bios

Spectral contrast imaging method for mapping transmission surface plasmon images in metallic nanostructures

Ming-Yang Pan[a], Deng-Kai Yang[b], Chih-Yu Lai[c], Jui-Hong Weng[c], Kuang-Li Lee[a], Lin-Chi Chen[c], Chia-Fu Chou[b], Pei-Kuen Wei[a,d,e,*]

[a] Research Center for Applied Sciences, Academia Sinica, Taipei, Taiwan
[b] Institute of Physics, Academia Sinica, Taipei, Taiwan
[c] Department of Bio-Industrial Mechatronics Engineering, National Taiwan University, Taipei, Taiwan
[d] Institute of Biophotonics, National Yang-Ming University, Taipei, Taiwan
[e] Department of Optoelectronics, National Taiwan Ocean University, Keelung, Taiwan

ARTICLE INFO

Keywords:
Surface plasmon resonance
Biointeractions
Metallic nanostructures
Spectral contrast method
Microfluidic devices

ABSTRACT

We propose a spectral contrast method to map the transmission images of surface plasmon resonance (SPR) in metallic nanostructures. Comparing the intensities between two neighboring wavelength bands near the SPR wavelength, the signal-to-noise ratio for biosensing applications obtained using the proposed method is found to be ten times higher than that obtained by conventional intensity analysis and 1.6 times better than that obtained by peak-wavelength fitting. The dynamic range and linearity of the refractive index are comparable to the peak-wavelength shift measurement. Based on the detection method, a spectral modulation system for the optical microscope is developed, combined with a gold-capped nanowire array, to measure the biointeractions in microfluidic devices. The experimental results show that the proposed method obtained multiple detections with a detection limit of 1.04×10^{-5} refractive index units. Two types of analysis methods for SPR images are used to study the protein-antibody interactions. The region-of-interest analysis supports multiplexing detections in a compact microfluidic sensor. The effective pixel analysis eliminates low-response pixels and enhances the signal-to-noise ratios for sensitive label-free detection.

1. Introduction

The surface plasmon resonance (SPR) sensing technique is well-known for its advantages of high-sensitivity, label-free, and real-time detection. Hundreds of SPR sensors have been developed and applied in clinical, biochemical, and environmental applications (Homola, 2008; Law et al., 2011; Masson, 2017; Olaru et al., 2015; Verma and Gupta, 2015). In many applications, the SPR sensors need to detect multiple targets or sense multiple probes using one target. Traditional prism-based SPR measurements, such as peak-wavelength or angle-scanning measurements, provide limited SPR channels and limit the throughput of detection. Therefore, the research is towards the development of systems capable of reading surface plasmonic signals in high-throughput applications. The SPR imaging technique resolves the wavevector parameters of surface plasmonic waves from different areas in an SPR sensor (Wong and Olivo, 2014). It allows the parallel monitoring of biomolecular interactions. Multiplex detections have been processed using SPR images for various purposes, such as DNA/RNA hybridization (Nelson et al., 2001), food safety (Piliarik et al., 2009), binding kinetics measurement (Campbell and Kim, 2007), small-molecule drug discovery (Zhou et al., 2018), diagnosis of disease (Castiello and Tabrizian, 2018), and aptamer assessment (Jia et al., 2018). In addition to the prism-based SPR sensors, chip-based metallic nanostructures offer a direct and simple way to excite SPR (Endo et al., 2006; Schwarz et al., 2014) and are more suitable for high-throughput sensing applications (Cetin et al., 2014; Aćimović et al., 2017). Different from the SPR in a prism-based sensor, the resonance in periodic metallic nanostructures arises from the coupling of the Bloch wave surface plasmon polariton (BW-SPP) mode and the localized modes in metallic nanostructures (López-Muñoz et al., 2017). Such a coupling usually forms a Fano resonance with an asymmetric profile, which sharpens the SPR spectrum and improves the detection sensitivity (Lee et al., 2015). A simple measurement method to map the Fano resonance image in metallic nanostructures is to use a laser or a narrow-band light source near the SPR wavelength. The light is normally incident on the nanostructures and the transmission optical image is recorded by a

* Corresponding author. Research Center for Applied Sciences, Academia Sinica, Taipei, Taiwan.
E-mail address: pkwei@gate.sinica.edu.tw (P.-K. Wei).

https://doi.org/10.1016/j.bios.2019.111545
Received 21 March 2019; Received in revised form 30 June 2019; Accepted 26 July 2019
Available online 28 July 2019
0956-5663/

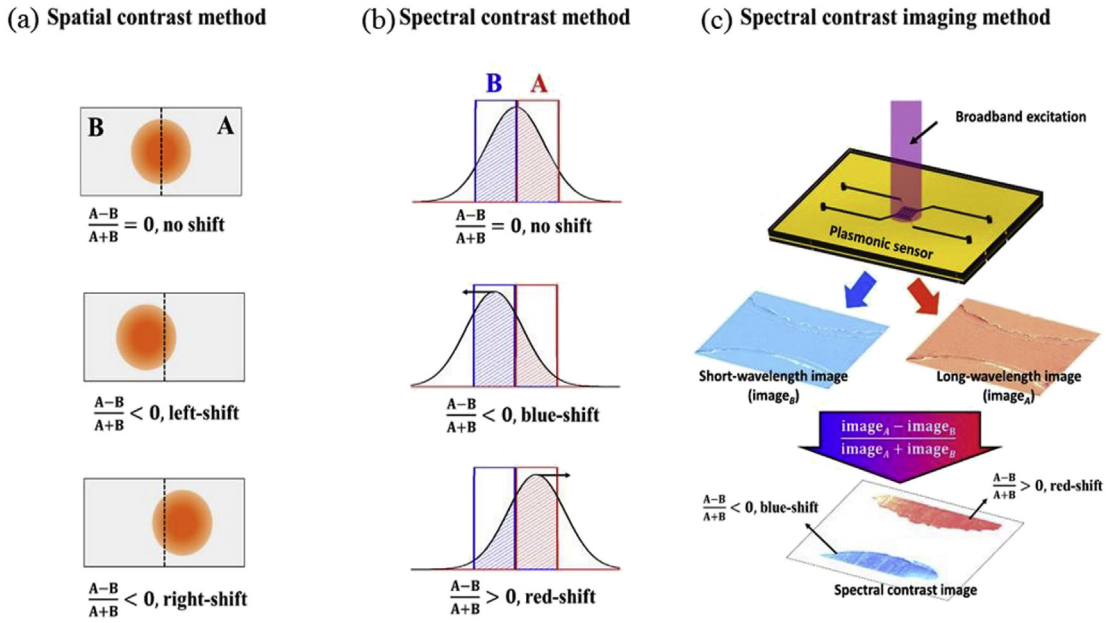

Fig. 1. Schematic illustration of the concept of using (a) spatial contrast method for beam position detection and (b) spectral contrast method for spectral peak shift detection. (c) The spatial contrast imaging method for SPR image.

camera (Lee et al., 2016). As the intensity interrogation method is sensitive to factors such as the light absorption of the analyte and the intensity noises in the light source and the detectors, the signal-to-noise (S/N) level is usually smaller than that in the peak-wavelength or the angle interrogation methods. The S/N level can be improved using a hyper-spectrometer with a motorized linear stage to scan the spectra for each image pixel (Tai et al., 2018). However, hyperspectral imaging is a time-consuming process which limits the temporal resolution. Moreover, the system is expensive due to the requirement of a hyper-spectrometer.

In this study, we propose a spectral contrast (SC) method to map the SPR images in gold nanostructures. The idea is derived from the beam position measurement used in the atomic force microscopy system (Andrew and Ludger, 2008). As shown in Fig. 1, the two segments of the sensor can sensitively measure the change in the central position of an incident beam; however, they are insensitive to the intensity fluctuation of the light source. In a resonant spectrum, two bandpass filters centered at the left and right of the resonant wavelength are analogous to the two segments of the position sensor. Fig. 1(b) shows that the contrast signal of both the transmission intensities is related to the shift in peak wavelength, analogous to the position change of a laser beam. The SC approach can be easily incorporated to record images using a charge-coupled device (CCD) and observe the difference in the spatial intensity from both the filters (Fig. 1(c)). The SC images related to the peak-wavelength shift and surface refractive index (RI) change are then measured. We theoretically and experimentally verify that the proposed method has a much higher S/N and better response linearity than the intensity interrogation method. We demonstrate this method by adding a spectral modulation system to an inverted optical microscope. A sensing device composed of microfluidic channels and gold-capped nanowire arrays is used to demonstrate the sensing performances. In addition, two analysis methods, region-of-interest (ROI) analysis and effective pixel analysis, are introduced to study protein-antibody dynamic interactions.

2. Materials and methods

2.1. Fabrication of the sensing device

The sensing device is composed of a nanoplasmonic sensing chip and a microfluidic component. The nanoplasmonic sensing chip consisting of periodic gold-capped nanowires is fabricated on COP plastic films (cyclo-olefin polymer, ZF14-188) by the hot-embossing nanoimprinting process (Lee et al., 2018), as shown in Fig. S1. The mold for nanoimprinting is fabricated by e-beam lithography and electrodeposition method. First, a layer of e-beam resist (ZEP-520a) is spin-coated onto a 525 μm-thick Si substrate. After being written with an e-beam writer (ELS-7000, Elionix) and the lift-off process, a nanowire array is fabricated on the resist. The designed period, nanowire width, and area are 470 nm, 70 nm, and 5 mm × 5 mm, respectively. This pattern is used as a template to form a Ni–Co mold by the electrodeposition process. Due to the pattern transfer process, a periodic nanogrooves pattern is obtained in the Ni–Co mold. After cleaning, the mold is installed on a home-made hot-embossing nanoimprinter. In the nanoimprinting process, the mold is heated to 180 °C, which is higher than the glass transition temperatures of COP (136 °C), and then embossed onto a plastic film for several minutes. After the cooling (set at 60 °C) and demolding process, the plastic films with nanowire array patterns are fabricated. To avoid environmental particles, the machine is installed in a clean room. To improve the accuracy and stability of the device, the sample is moved by motorized translational stages. This imprinting system has the advantages of low-cost and mass fabrication. Fig. S1(b) presents the optical images of 96 patterns of nanowire arrays on the COP film. Fig. S2(a) presents the scanning electron microscope (SEM) image of the imprinted nanowire array. The period and nanowire width are consistent with the designed pattern. Fig. S2(b) presents the atomic force microscope (AFM) image. The height of the nanowire array is approximately 60 nm as seen in Fig. S2(c). The imprinted chip is deposited with a 50-nm-thick gold film using DC sputtering to form gold-capped nanowire arrays. The nanowire array is employed as the SPR sensing chip. The uniformity of the nanowires plays an important role on the sensitivity of gold–capped nanowire arrays. As seen in Supplementary Fig. S1(d), the photo image shows good uniformity of diffraction colors caused by the periodic gold–capped nanowires. The SEM and AFM images also indicate good uniformity of the nanostructures. The root-mean-square roughness after the gold deposition is 1.9 nm, as shown in Fig. S2(d). Compared to the height of the nanowires, the gold roughness has a minor effect on the transmission spectra. A double-sided tape (4905 VHB^{TM}, 3 M) with fluidic channels is used to bind the sensing chip and the polymethylmetacrylate (PMMA)

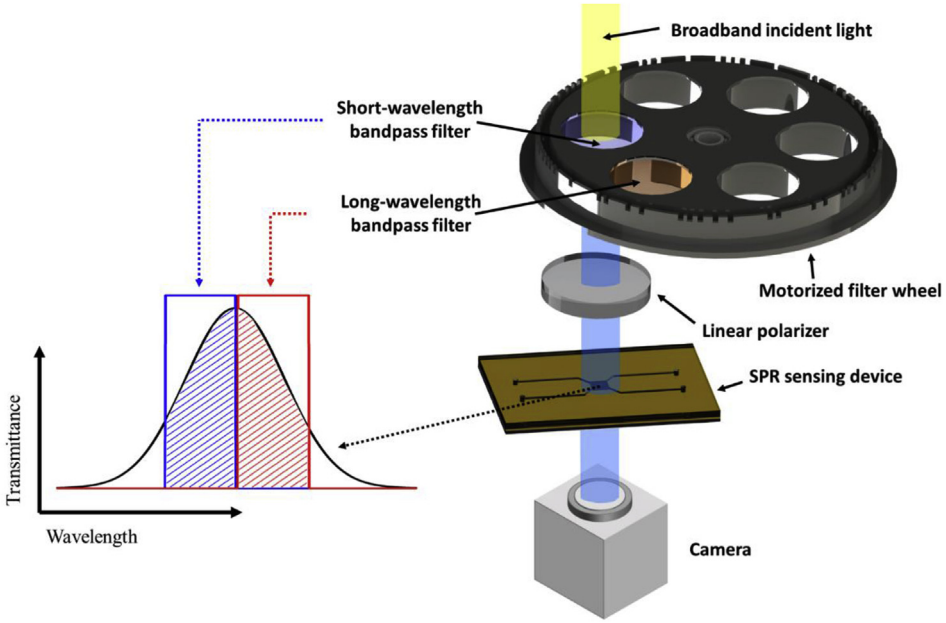

Fig. 2. Schematic of the SC-SPR imaging system. Two bandpass filters are mounted on a motorized filter wheel. The spectral band is modulated by rotating the filter wheel. The components of the microscope such as objective, lens, and mirror are not shown in this figure.

cover. Figs. S3(a) and 3(b) present the layouts of the chip and a photograph of the sensing device used in the sensing experiments.

2.2. Spectral contrast SPR imaging system

Fig. 2 illustrates the optical setup of the SC imaging system. It is built on an inverted microscope (IX71, Olympus). A normal incident illumination system with a broadband light source (SLS201, Thorlabs) replaced the built-in illumination system of the microscope. The light is passed through a spectral modulation system composed of a motorized filter wheel (FW102C, Thorlabs) with two different bandpass filters (ET640 and ZET660, Chroma). The bandwidths of both the bandpass filters are 20 nm. The long and short cutoff wavelengths of both the filters are near the resonant wavelength of the gold-capped nanowire array. The filtered light is passed through a linear polarizer and is incident onto the sensing device. The transmission light is imaged by a 12-bit CMOS camera (C11440, Hamamatsu). The motorized filter wheel is controlled by a customized LabVIEW program to alternately change the filter; this is synchronically recorded by the camera.

2.3. Measurement of transmission spectra

To compare the performance of the SC imaging method with the conventional peak-wavelength shift and intensity change methods, the transmission spectra of the sensing device are measured by a spectroscopic system. Similar to the imaging system, the device is placed on the microscope and illuminated by a normally incident and linearly polarized light. However, different from the resonance imaging method, the transmitted light is directly collected by an objective and then sent into a spectrometer (BTC112, B&W Tek).

2.4. Calculation of the spectral contrast image

The images obtained by the camera are categorized into two spectral parts. The image excited by the light passing through the longer wavelength bandpass filter is defined as the long-wavelength image, $image_A$. In the same way, the image excited by the light passing through the shorter wavelength bandpass filter is defined as the short-wavelength image, $image_B$. Using both the images, the SC response (γ) for each image pixel is calculated by the following formula:

$$\gamma(m, n, t) = \frac{[image_A(m, n, t) - image_B(m, n, t)]}{[image_A(m, n, t) + image_B(m, n, t)]}, \quad (1)$$

where m and n denote the pixel position of the image, and t is the time duration of biointeractions. Thus, the position-dependent SC responses can be extracted from these images. The maximum frame rate of an SC response image is approximately 1/3 fps (frames per second), which is limited by the rotation speed of the motorized filter wheel.

2.5. Preparation of the analyte

For experimental measurement of the sensitivity and LoD, we use a series of different concentrations of glucose/water solutions. A 5% (w/w) glucose/water solution is first prepared. Other concentrations, namely, 2.5%, 1.25%, 0.625%, and 0.3125% glucose/water solution, are prepared by diluting the mixtures with deionized water. The refractive indices (RIs) of those mixtures are measured by a refractometer (DFR, MISCO). For the biosensing experiments, bovine serum albumin (BSA, 66 kDa, Sigma-Aldrich), bovine serum albumin antibody (anti-BSA, 150 kDa, Sigma-Aldrich), and immunoglobulin A antibody (anti-IgA, Bethyl Laboratories) are prepared in 10 mM phosphatebuffered saline (PBS) buffers. Mouse anti-MUC1 antibody (Anti-MUC1, C595, 122kDa, Abcam) recognizes the peptide epitope ARG-PRO-ALA-PRO (RPAP) within the protein core of MUC1. His-tagged MUC1 peptide (MUC1, 1703.79 Da, GenScript) is composed of 15 amino acids (HHHHHHAPDTRPAPG). Human serum albumin (HSA, 66 kDa, Sigma-Aldrich), nickel(II) chloride hexahydrate ($NiCl_2$, 237.69 Da, Sigma-Aldrich), mouse anti-MUC1 antibody, and His-tagged MUC1 peptide, are prepared in running buffer, which contains 1 × HBS-P buffer (GE Healthcare) and 50uM ethylenediaminetetraacetic acid (EDTA, 0.5 M, pH8, Invitrogen).

2.6. Surface modification of the sensing chip

In the anti-MUC1 biointeraction experiment, the COP film is chosen as the substrate for its excellent chemical solvent resistance. To modify the nitrilotriacetic acid (NTA) group on an Au/COP chip, N-[Nα,Nα-Bis (carboxymethyl)-L-lysine]-16-mercaptohexadecanamide (SH-NTA, 0.2 mg mL-1) is first prepared in dimethyl sulfoxide (DMSO, Sigma-Aldrich) and then dropped onto the nanoimprinted Au/COP chip. After

overnight incubation, 10 mM 11-mercaptoundecanoic acid (MUDA, Sigma-Aldrich) in DMSO is used to passivate the unreacted Au surface. After 1-h reaction time, the chip is rinsed by deionized water, dried by N_2 gas, and sealed with a microfluidic chip. This NTA-functionalized sensing device can be activated by Ni ion. The His-tagged peptide can be captured by the metal of metal chelator complexes such as Ni-NTA.

3. Results and discussion

3.1. Theoretical analysis of the spectral contrast imaging method

The periodic metallic nanostructures show excellent sensing performances according to their extraordinary optical transmission (EOT) property. The EOT caused by the SPR mode results in a transmission peak at a specific wavelength, which is sensitive to the effective surface RI (Ebbesen et al., 1998). The resonant wavelength of the SPR mode is estimated by the wavevector matching condition:

$$\lambda_{SPP} = \frac{P}{i}\sqrt{\frac{\varepsilon_m n_s^2}{\varepsilon_m + n_s^2}}, \quad (2)$$

where P is the period, i is the resonance order, ε_m is the dielectric constant of the metal, and n_s is the effective RI on the sensor surface. As indicated in Eq. (2), the resonant wavelength of the SPR mode in periodic nanostructures is determined by the period, metal and surface refractive index. In our experiments, the period is 470 nm and the metal is gold. The estimated SPR wavelength in water is ~660 nm, which is close to the measured value, 650 nm. The binding events increase the surface refractive index, therefore the SPR wavelength is red-shifted. On the other hand, the dissociation events decrease the n_s and the SPR wavelength is blue-shifted. The nanostructure used in this study is a gold-capped nanowire array. The localized resonance in the gold nanowires causes a broadband resonance in the transmission spectrum. When the resonance has an overlapping with the SPR mode, the coupling of both the modes results in Fano resonance. A simple Fano resonance profile can be described by the following equation (Lee et al., 2015):

$$T = \frac{(q+\delta)^2}{1+\delta^2}, \quad (3)$$

where $\delta = \frac{(\lambda^{-1} - \lambda_{spp}^{-1})}{\gamma_{spp}}$, q is the Fano factor describing the coupling degree between the SPR and cavity modes, δ is the normalized frequency at the top metallic surface, λ_{spp} is the resonant wavelength of the SPR mode, and γ_{spp} is the damping factor. Fig. 3(a) shows the calculated Fano resonance for this experiment. The fitting parameters for q, λ_{spp}, and γ_{spp} are -5, 640 nm, and 3.3×10^{-5}, respectively.

To verify the performance, we theoretically calculate the S/N and dynamic range with the SC analysis, peak wavelength shift (Δλ), and intensity change (ΔI) methods for the Fano resonance profile. To simulate the noise effect, pseudorandom values drawn from the standard normal distribution are generated using a MATLAB code, *randn()*. Different standard deviations of noises are added to the transmission spectrum. The transmission spectrum has a resonance peak at 650 nm. To calculate the SPR responses for the different analytical methods, the resonant wavelength is shifted from −2.5–7.5 nm, i.e., the peak wavelength is shifted from 647.5 to 657.5 nm. The SC method has a γ value as calculated by Equation (1). The peak wavelength in the wavelength interrogation method is obtained using a Gaussian fitting near the peak wavelength. The intensity change is calculated at 640 nm wavelength with 1 nm bandwidth. Fig. 3(b) presents the response as a function of time for the different shifted values of the spectra. The bandwidth of the bandpass filter is 20 nm and the noise level is 1%. It is obvious that the γ value has a better S/N than the responses of Δλ and ΔI. Thus, the bandwidth of the bandpass filter plays an important role in the S/N value. Fig. 3(c) presents the S/N values for different bandwidths from 10 to 40 nm. The average signals and noises are obtained from Fig. 3(b) for different noise levels from 1% to 5%. The maximum S/N occurs at a bandwidth of 20 nm, which is close to the half-bandwidth (~25 nm) of the Fano resonance. Compared to the S/N values obtained from peak-wavelength fitting and intensity change, the S/N of the 20-nm-bandwidth SC method is improved by factors of 1.6 and 6.4, respectively. Fig. 3(d) presents the average signal response as a function of the resonant wavelength shift. We observe a linear correlation between the response and the peak-wavelength shift. Moreover, the SC method preserves a good linearity. The theoretical study shows that the SC analysis has a better S/N value, good linear response, and large dynamic range.

3.2. Experimental sensitivity and limit of detection

To experimentally verify the sensitivity and LoD, glucose/water solutions with known RIs are used as the analyte to test the SC responses. These solutions are injected into the sensing device in sequence, and the corresponding spectra and SC images are recorded. For comparison, intensity and peak-wavelength interrogations are also used to analyze these spectra. The sensitivities and LoDs are determined by measuring the responses for the different RIs. The signals are calculated by averaging the responses in each RI step, and the noises are calculated from the standard deviations of the signals. Fig. 4(a) presents the spectra for these solutions. The peak wavelength is red-shifted due to the increase in the RI of the solution. Fig. 4(b) presents the intensity interrogation at 651.8 nm wavelength. We observe that the signals increase with the RI and the noises are quite large. The sensitivity is 157.63 a.u. RIU^{-1}, and the standard deviation of the noise level is 2.92×10^{-2} a.u. This indicates that the LoD of the intensity method is only 1.85×10^{-4} RIU. Fig. 4(c) presents the peak-wavelength sensorgram as measured by the spectroscopic system with the peak-wavelength fitting method. For the SC imaging method, the time-sequence SC images are recorded and only the signals in the gold-capped nanowire array are calculated. Fig. 4(d) presents the SC response for different RIs. The two sensorgrams show similar responses and have much lower noises than the intensity method. The sensorgram measured by the SC imaging system is more stable and less noisy than that measured by the peak-wavelength method for all the RI steps. Fig. 4(e) and (f) summarize the measured signals as a function of RI. Both responses show very good linearity for all the RI changes. For the spectral measurement, the peak wavelength is red-shifted from 645 to 647.21 nm. The wavelength sensitivity is 346.42 nm RIU^{-1}. Considering a noise level of 5.8×10^{-3} nm in pure water, the LoD is 1.67×10^{-5} RIU. For the SC imaging measurement, the sensitivity is 10.8558 a.u. RIU^{-1} and the measured noise is 1.1277×10^{-4}. The LoD is 1.04×10^{-5} RIU, better than that in the wavelength fitting method. It should be noted that the pixel depth of the camera used in the SC imaging system is only 12 bit, which is lower than the 16 bit spectrometer. The sensors, optical measurement devices used in this study, and sensing performances for the different interrogation approaches are summarized in Table 1. For the proposed SC method, the LoD is 1.6 times lower than that in the traditional spectral measurement and one order of magnitude better than that in the intensity method. The improvement in S/N as compared to the wavelength fitting and intensity methods are closer to the theoretical estimates.

3.3. Region-of-interest analysis

The SC imaging method provides a useful way to measure biomolecular interactions in microfluidic devices. In traditional spectroscopic measurements, the size of the sensing area should be larger than an incident light beam and arranged inside the fluidic channel. Otherwise, the signal is reduced by the no-response region. This limits some fluidic applications which need compact microfluidic structures (Karle et al., 2016; Sajeesh and Sen, 2014). The SC image configuration is based on a comparison between filtered images. The signals can be directly

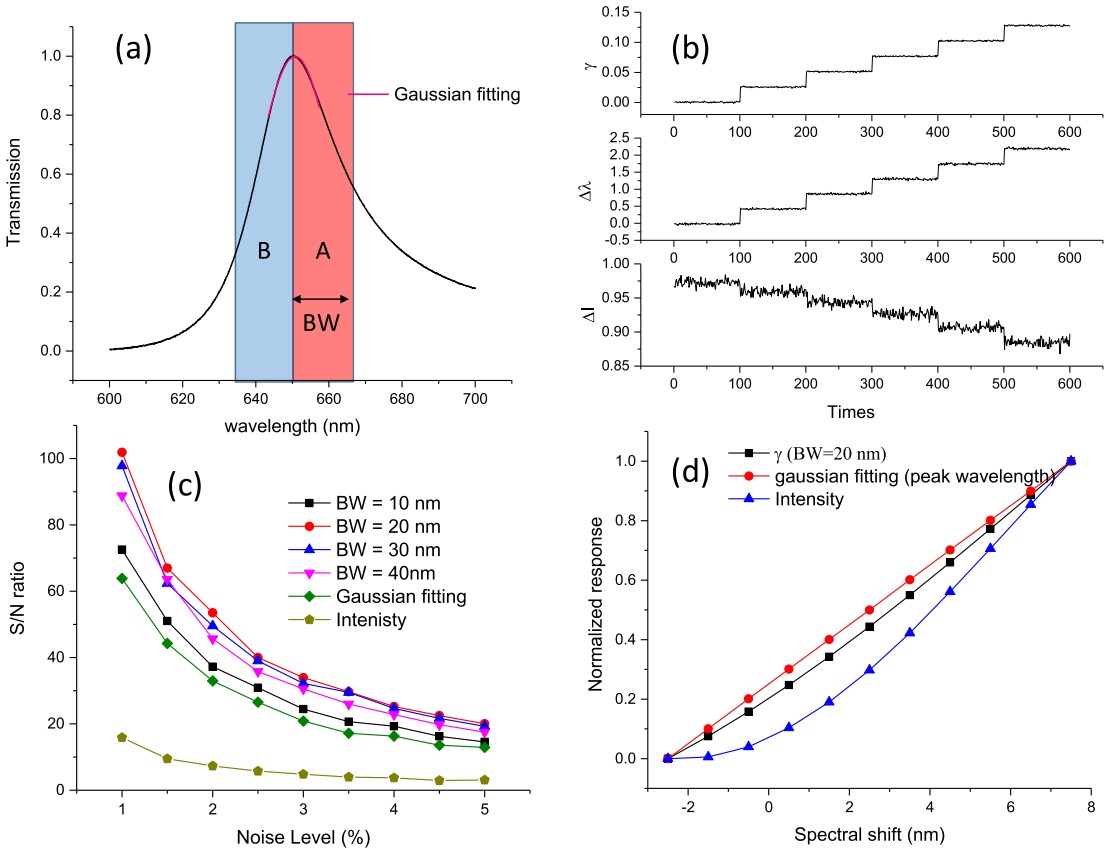

Fig. 3. Theoretical comparisons of the sensing performance by using SC, wavelength, and intensity interrogations. (a) Calculated Fano-resonance spectrum (black-line) and bandwidth (BW) of the optical filter (red: long-wavelength bandpass filter, blue: short-wavelength bandpass filter). The red-line shows the Gaussian fitting for the peak. (b) The calculated signal responses by using SC (top), peak wavelength shift (middle), and intensity change (bottom) methods. (c) The S/N ratios for various noise levels in the spectra and analyzed by different interrogation methods. (d) The calculated signal responses as a function of the spectral shift. (For interpretation of the references to color in this figure legend, the reader is referred to the Web version of this article.)

extracted from any area in the measured images. Fig. 5(a) presents an example of a protein-antibody interaction measured by the SC imaging method. The size of the gold-capped nanowire array is 5 mm × 5 mm. A fluidic channel is placed on the nanostructure array. 0.5 × and 1 × PBS buffers are first injected into the fluidic channels in order to identify the sensing area. As shown in the Supplementary Movie S1, only the area which is overlapped with the gold-capped nanowire array and the fluidic channels show signal responses. Since the sensing area has been identified. The sensorgram of the molecular interactions is directly extracted from this area. Fig. 5(b) presents the sensorgram analyzed from the SC images. The difference in the SC response is defined as $\Delta\gamma(t) = \gamma(t) - \gamma(0)$. The black, red, and blue lines show the averaged signals extracted from the black, red, and blue squares, respectively.

Supplementary data related to this article can be found at https://doi.org/10.1016/j.bios.2019.111545.

In the black-squared area, the SC value increases to 6×10^{-3} a.u. due to the increase in PBS concentration. This helps us to identify the sensing area. The PBS buffer is injected into the fluidic channel with a flowrate of 20 μL min^{-1} for 20 min to ensure that the fluidic channel has immersed in the buffer solution. Following this step, 50 μg mL^{-1} BSA dissolved in the PBS buffer is injected into the fluidic channel with a flowrate of 10 μL min^{-1} for 40 min. The BSA molecules are immobilized onto the sensor surface due to the binding between the gold surface and the free thiol groups in BSA molecules. After washing the non-adsorbed BSA molecules by PBS washing, $\Delta\gamma$ increases to 1.04×10^{-2}. To check the specificity of the BSA-mobilized sensor, 50 μg mL^{-1} anti-IgA is injected into the sensor with a flowrate of 10 μL min^{-1} for 40 min. No increase in the signals is observed for the non-specific binding. For a target analyte of 50 μg mL^{-1} anti-BSA with a flowrate of 10 μL min^{-1} for 40 min, $\Delta\gamma$ rapidly increases to 5.88×10^{-2} a.u. and slowly decreases to 5.65×10^{-2} a.u. during the 40-min PBS washing step. In contrast, no responses are observed in the other selected areas such as the blue-squared area (out of the fluidic channel) and the red-squared area (in the fluidic channel but without the gold nanostructures). To further study the interference effect, we inject various target analytes into the BSA coated surface for four different channels as shown in Fig. 5(c). The high concentration anti-IgG shows an abrupt increase of signals due to the increase of bulk refractive index. After PBS washing, the signals rapidly drop to the base line. The increase of $\Delta\gamma$ as compared to the BSA surface is only 2×10^{-4}. For anti-BSA samples, the 20 and 10 μg mL^{-1} concentrations show slowly increase of the signals. After PBS washing, the increase of $\Delta\gamma$ come to 3.87×10^{-2} and 2.49×10^{-2}, respectively. For 10 μg mL^{-1} anti-BSA with 50 μg mL^{-1} anti-IgG, the signals show very similar response with the 10 μg mL^{-1} anti-BSA sample. These results indicate highly specific binding between BSA/anti-BSA and low interference of anti-IgG biomolecules.

The SC method is very useful for multiplex sensing in a microfluidic device. The inset in Fig. 5(d) presents a four-channel sensing device using the 5 mm × 5 mm Fano sensing chip, which is analyzed by the SC method. The Supplementary Movie S2 demonstrates the simultaneous measurement of four different concentrations of antigen-antibody interactions. All the channels are first modified with 1 mg mL^{-1} of BSA for approximately 20 min. Next, the fluidic channels are PBS-washed for approximately 20 min to remove the unbound BSA molecules. Different concentrations, 0, 100, 10, and 1 μg mL^{-1}, of anti-BSA are then injected into the first, second, third, and fourth channels, respectively. The unbound anti-BSA are removed by PBS washing for 20 min.

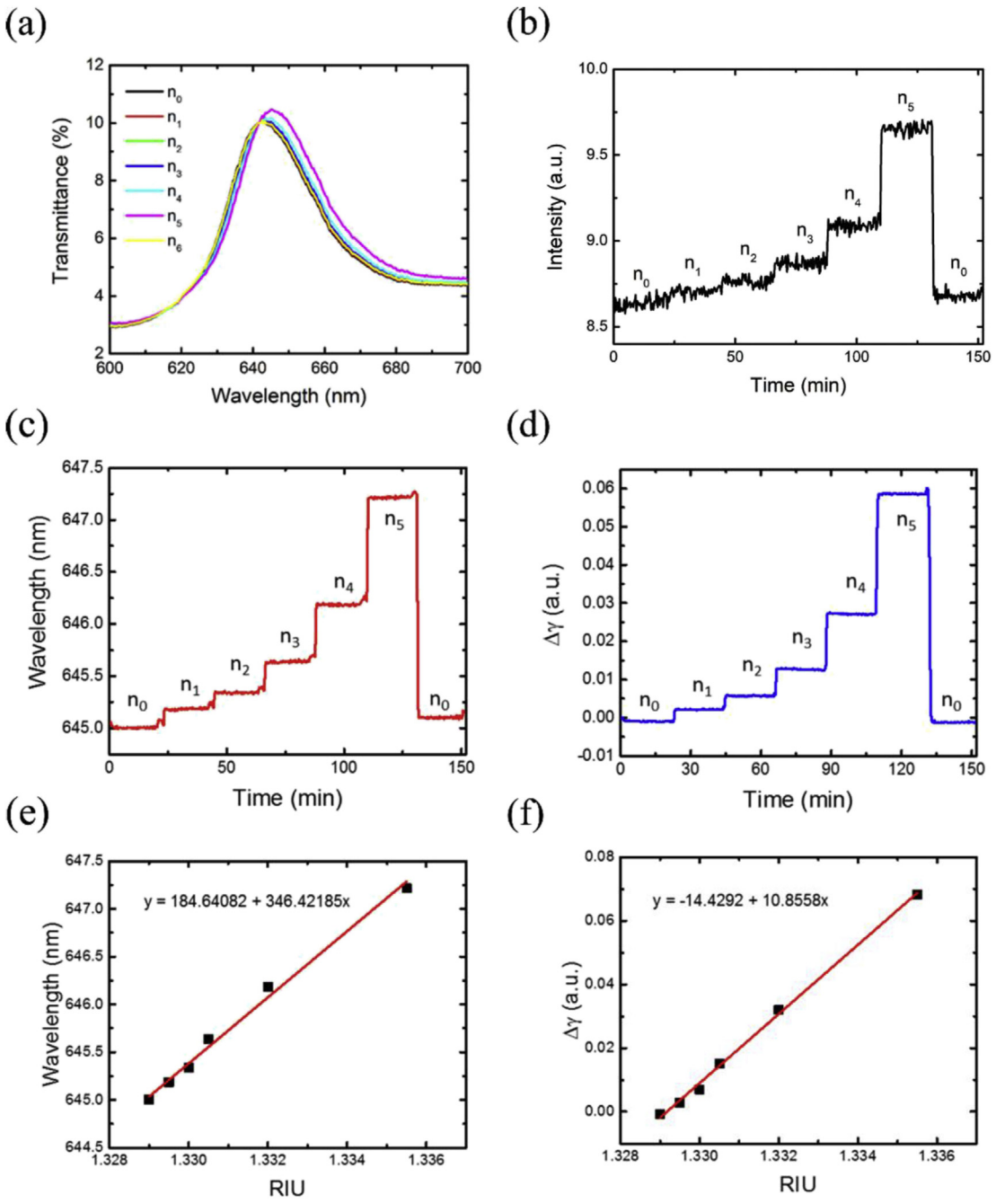

Fig. 4. Sensitivity and LoD determinations for spectroscopic measurement with peak-wavelength, intensity interrogation methods and SPR image measurement with the SC method. (a) The measured transmission spectra, (b) the time-dependent intensity changes at 651.8 nm of wavelength, (c) the peak wavelengths, and (d) SC responses for various concentrations of glucose/water solutions. The RIUs of n_0 to n_6 are 1.329, 1.3295, 1.33, 1.3305, 1.332, and 1.3355, respectively. (e) The peak wavelengths and (f) the SC signals as a function of RIU. The noises are calculated form the standard deviations of measured signals in each steps and presented as error bars but cannot be seen because they are too small. The slopes of the fitting curves show that the sensitivity were 346.42185 nm RIU^{-1} and 10.8558 a.u. RIU^{-1} by using spectroscopic and SC imaging measurement, respectively.

Table 1
A summary of different analytic methods and their sensing performances implemented in this work.

Analysis approach	Intensity interrogation	Wavelength interrogation	Spectral contrast method
Sensor	Gold-capped nanowires array	Gold-capped nanowires array	Gold-capped nanowires array
Optical measurement device	16-bits linear CCD-based spectrometer with ~0.4 nm wavelength resolution	16-bits linear CCD-based spectrometer with ~0.4 nm wavelength resolution	12-bits 1920 × 1440 CMOS camera
Field-of-view	Single spot with 200μm diameter	Single spot with 200μm diamete	~5 mm × 4 mm
Sensitivity	157.6326 a.u. RIU^{-1}	346.42 nm RIU^{-1}	10.8558 a.u. RIU^{-1}
Noise	0.0292 a.u.	5.8×10^{-3} nm	1.1277×10^{-4} a.u.
LoD	1.85×10^{-4} RIU	1.67×10^{-5} RIU	1.04×10^{-5} RIU

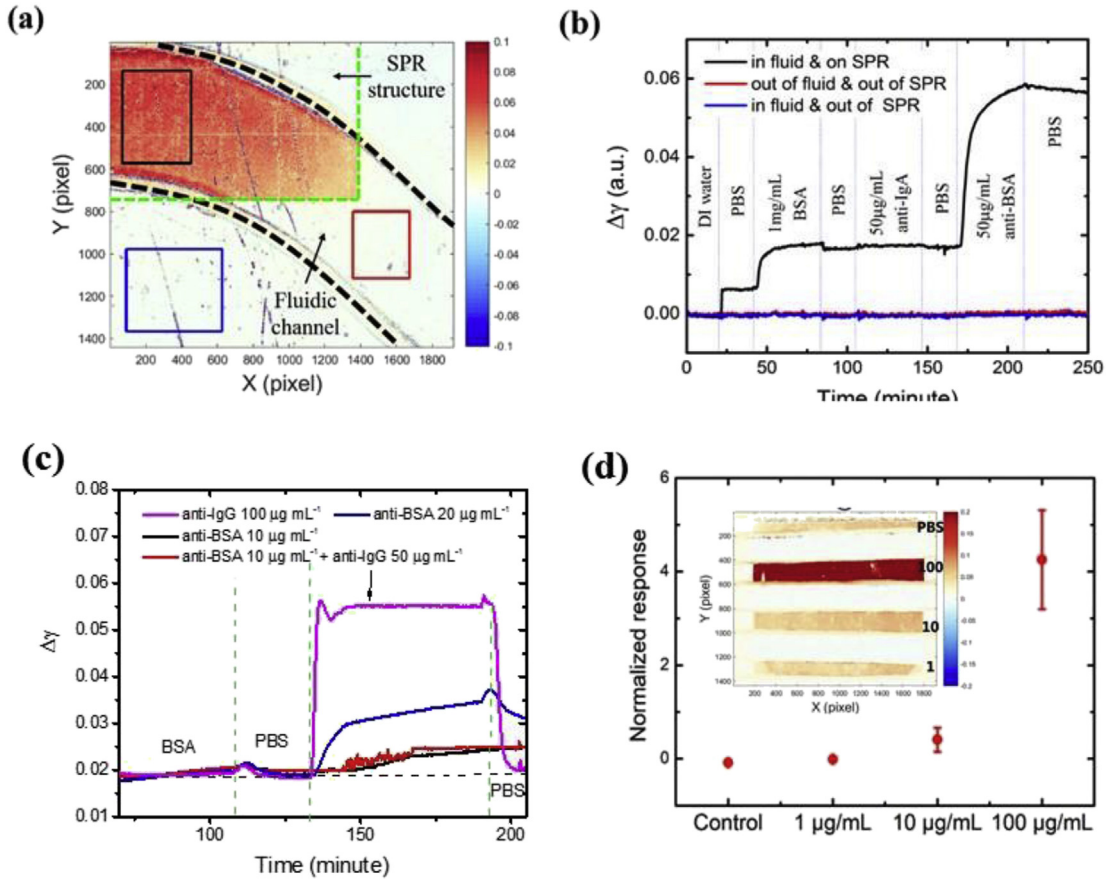

Fig. 5. Region of interest analysis. (a) The measured spectral contrast image. The gold-capped nanowire array is located inside the green dashed line. The fluidic channel is indicated by black dashed lines. (b) The measured sensorgrams analyzed by the averaged signals in the black, red and blue squares. (c) The measured sensorgrams for different proteins and mixture. (d) The measured responses as a function of anti-BSA concentration from 1 μg mL^{-1} to 100 mL^{-1}. The error bars indicate the standard deviations of measured responses from three sensing chips. (For interpretation of the references to color in this figure legend, the reader is referred to the Web version of this article.)

Fig. 5(d) summarizes the calculated SC responses for different sensing chips. We have tested three different chips. Each chip has four channels. The response values are calculated by the averaged value in the last 5 min, and the error bars denote the standard deviations for the different sensing chips. The responses are normalized to the signals of BSA modification by $\frac{\gamma anti-BSA-\gamma BSA}{\gamma BSA}$. The error bar in the control and 1 μg mL^{-1} sample are small. It indicates that these chips have good reproducibility. A larger deviation occurs for a higher concentration of anti-BSA. We attribute the large deviation to the formation of multiple anti-BSA layers. When binding sites of BSA are fully occupied by the anti-BSA, the excessive anti-BSA would continuously deposit on the surface. The remained amount of anti-BSA after PBS washing would have a large difference.

Supplementary data related to this article can be found at https://doi.org/10.1016/j.bios.2019.111545.

3.4. Effective pixel analysis

In the fabrication of nanostructure-based plasmonic sensors such as nanoholes, nanoslit arrays, and nanoparticle arrays, there might be non-uniform areas or defects. These defects have small sensitivities or even no responses to surface RI change. The signal is under-valued when these areas are involved in the measurement. To exclude the defect areas and enhance the signals, we propose an effective pixel analysis method for nulling out the areas with low sensitivities. The effective pixel analysis method follows the following steps: (1) SC image calibration, (2) histogram and threshold setting, (3) spatial mask generation, and (4) applying the spatial mask to the measured SC images. Fig. 6 illustrates the concept of effective pixel analysis. A dual-fluidic channel with a gold-capped nanowire array is used as the sensing device. To demonstrate the advantage of the effective pixel analysis, the nanowire array chip is chosen with some non-uniformities. In the experiment, the PBS buffer (1X) is first injected into the fluidic channels. The distribution of the SC response is shown as a histogram (Fig. 6(a)). A distribution with a central value of zero is observed. Next, a calibration solution with a high concentration of PBS (5X) is injected into the fluidic channels to cause higher responses. The histogram in Fig. 6(b) shows that the SC responses are split into two peaks. The second peak denotes the pixels sensitive to the RI changes. Using normal distribution fitting, the central response, γ_c, and the standard deviation, γ_w, are calculated for the second peak. Fig. 6(c) presents the map of the pixels where the measured values for the calibration solution are in the range of $\gamma_c \pm \gamma_w$. The pixels in this range are denoted as the effective pixels. The effective pixels (defined as one) and the other pixels (defined as zero) are employed as a spatial mask, as shown in Fig. 6(d). Fig. 6(e) and (f) present the measured SC images without/with applying the effective pixel mask, respectively. Fig. 6(g) presents the sensorgram without/with the effective pixel analysis. In this experiment, an NTA-mobilized sensing device with a dual-fluidic channel is used to detect anti-MUC1. The microfluidic channels consist of a control channel (top: Ctrl-channel) and an experiment channel (bottom: Exp-channel). Before immobilizing the His-tagged-MUC1 peptide, 1 mg mL-1 HSA is injected into both the channels to passivate the sensing area further. Non-adsorbed HSA molecules are removed by washing with the running buffer. Subsequently, the running buffer is continually injected into the Ctrl-channel. Meanwhile, 50 mM $NiCl_2$ is injected into

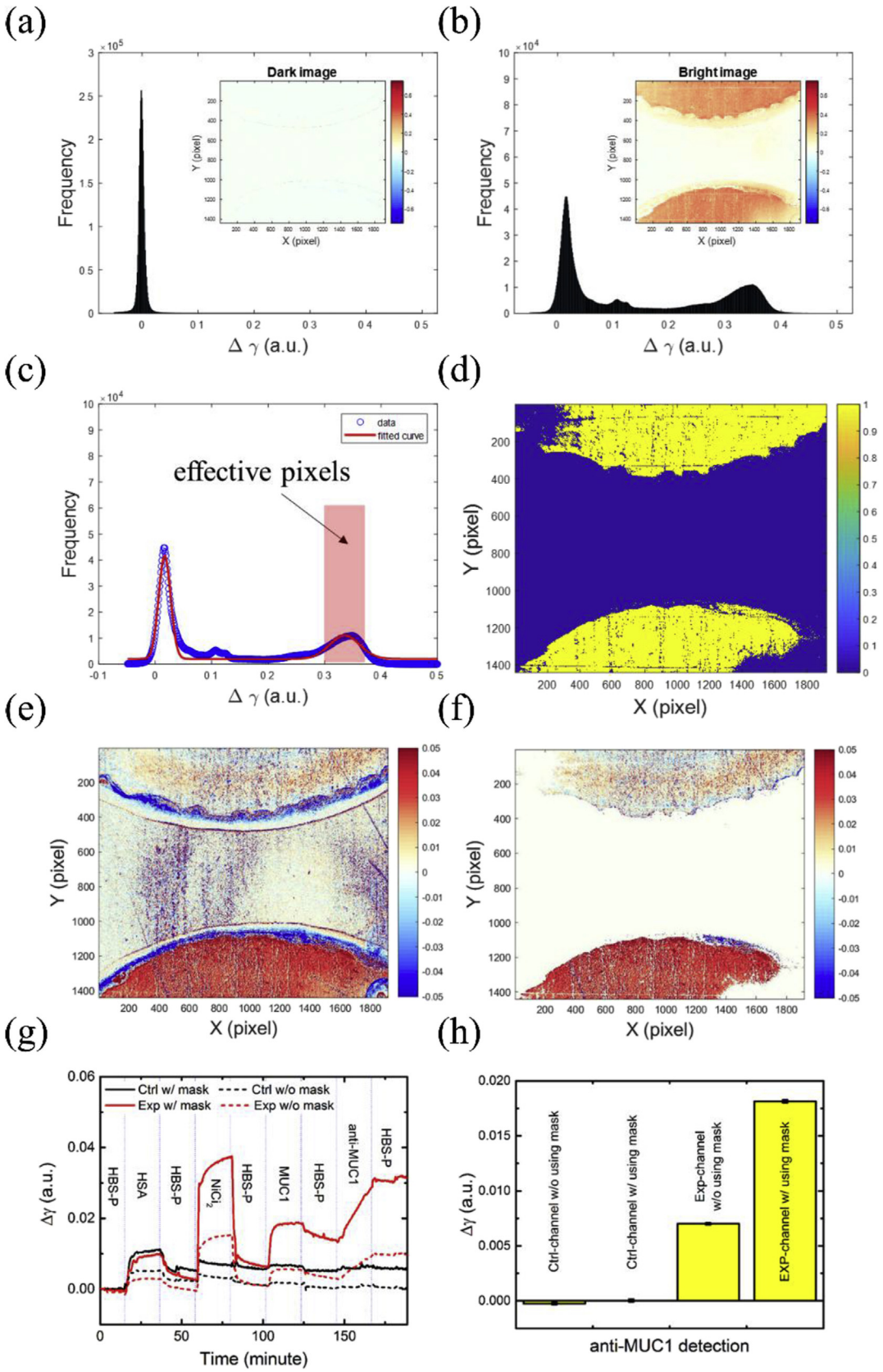

Fig. 6. Effective pixel analysis. (a) Initial SC image (inset figure) and the corresponding histogram. (b) The SC image (inset figure) and the corresponding histogram under high-RI solution for the calibration. (c) Effective pixels analyzed by histogram fitting. The blue-circles are measured data. The red-line denotes the fitting curve. (d) The effective pixel mask which considered as a binary filter for the measured SC images. The SC images without (e) and with (f) the effective pixel mask. (g) The measured sensorgrams of the control and experiment channels with (solid line) and without (dash line) the effective pixel mask. (h) The signals from interactions between MUC1 and anti-MUC1 in the control and experiment channels with/without the effective pixel mask. Error bars denote standard deviations of measured responses. (For interpretation of the references to color in this figure legend, the reader is referred to the Web version of this article.)

the Exp-channel to activate the NTA-modified gold surface. After the surface activation step, the channels are rewashed by the running buffer. 20 mM His-tagged-MUC1 peptide is then injected into both the channels. The uncaptured His-tagged-MUC1 peptide is removed by the running buffer. Next, 4 μg mL^{-1} anti-MUC1 antibodies are injected into both the channels to test the biointeractions. Finally, the unbounded antibodies are washed off by the running buffer. The injection flow rates in all of the running buffer steps are set to 20 μL min^{-1}. The injection flow rates in the other steps such as HSA, $NiCl_2$, MUC1, and anti-MUC1 are set to 10 μL min^{-1}.

The Supplementary Movie S3 presents the MUC1 detection using the SC image method. The SC images are divided into top and bottom parts representing control and experimental signals, respectively. Observably, both the control and experiment channels counted by effective pixel analysis has higher signals. Fig. 6(h) presents the measured anti-MUC1 detection signals. The experimental responses with/without effective pixel analysis are 1.815×10^{-2} and 0.7×10^{-2} a.u., respectively. Considering the related noise levels of 1.22×10^{-4} and 8.44×10^{-5} a.u., the S/N increases from 83.12 to 148.07 after applying the effective pixel mask. The effective pixel analysis not only improves the S/N but also provides a method for checking the uniformity and sensitivity of the nanostructure-based plasmonic sensor. It can be used as a method for quality control in the fabrication process of sensing chips. It is noted that this SC method has similar responses with the conventional peak-wavelength measurement using a spectrometer. In our recent study, we demonstrated by spectral measurement that the sensing chips can be used for real samples such as urine (Yeung et al., 2018). Therefore, the proposed SC method combined with the chips has a good potential in the detection of multiple target molecules in real samples.

Supplementary data related to this article can be found at https://doi.org/10.1016/j.bios.2019.111545.

4. Conclusions

In conclusion, we presented a spectral contrast imaging method for providing high-sensitivity, multiplex, and quick detection of transmission-type plasmonic sensing chips. The theoretical and experimental analyses showed that this method has a better S/N performance than the conventional intensity and wavelength interrogation methods. The experimental results showed that the SC image achieved 1.04×10^{-5} RIU resolution for the gold-capped nanowire arrays. Two analysis methods for the SC-SPR images were suggested and demonstrated. The region-of-interest analysis supports the simultaneous measurement of multiple signals in different regions. BSA, anti-BSA and anti-IgG biomolecules were used to demonstrate the specific binding and statistical results. The effective pixel analysis effectively increases the detection sensitivity by removing the low-response and defect areas. We used MUC1 and anti-MUC1 to show that the proposed SC method and sensors can be used for studying various antigen-antibody interactions. In this study, the SC imaging method was used for a transmission-type nanostructure-based plasmonic sensor. It can also be applied for reflection-type label-free sensing chips such as nanoparticle-based localized SPR chips and biolayer interferometry (BLI) sensors.

Declaration of competing interest

The authors declare that they have no known competing financial interests or personal relationships that could have appeared to influence the work reported in this paper.

The authors declare the following financial interests/personal relationships which may be considered as potential competing interests:

CRediT authorship contribution statement

Ming-Yang Pan: Conceptualization, Data curation, Investigation, Formal analysis, Writing - original draft. **Deng-Kai Yang:** Conceptualization, Data curation, Resources, Validation. **Chih-Yu Lai:** Resources, Validation. **Jui-Hong Weng:** Resources, Validation. **Kuang-Li Lee:** Methodology, Resources. **Lin-Chi Chen:** Conceptualization, Resources. **Chia-Fu Chou:** Project administration, Resources, Validation. **Pei-Kuen Wei:** Conceptualization, Funding acquisition, Project administration, Software, Supervision, Writing - review & editing.

Acknowledgement

This work was supported by the Ministry of Science and Technology (MOST) and Academia Sinica (AS), Taiwan, under Contract no. MOST 106-2627-B-001-001, AS - 106 - TP - A03 and AS-KPQ-106-TSPA. Technical support from the nano/micro-fabrication facilities in Academia Sinica is acknowledged.

Appendix A. Supplementary data

Supplementary data to this article can be found online at https://doi.org/10.1016/j.bios.2019.111545.

References

Aćimović, S.S., Šípová, H., Emilsson, G., Dahlin, A.B., Antosiewicz, T.J., Käll, M., 2017. Light Sci. Appl. 6, e17042.
Andrew, Y., Ludger, K., 2008. J. Phys. D 41, 103001.
Campbell, C.T., Kim, G., 2007. Biomaterials 28, 2380–2392.
Castiello, F.R., Tabrizian, M., 2018. Anal. Chem. 90, 3132–3139.
Cetin, A.E., Coskun, A.F., Galarreta, B.C., Huang, M., Herman, D., Ozcan, A., Altug, H., 2014. Light Sci. Appl. 3, e122.
Ebbesen, T.W., Lezec, H.J., Ghaemi, H.F., Thio, T., Wolff, P.A., 1998. Nature 391 (6668), 667–669.
Endo, T., Kerman, K., Nagatani, N., Hiepa, H.M., Kim, D.-K., Yonezawa, Y., Nakano, K., Tamiya, E., 2006. Anal. Chem. 78 (18), 6465–6475.
Homola, J., 2008. Chem. Rev. 108, 462–493.
Jia, W., Li, H., Wilkop, T., Liu, X., Yu, X., Cheng, Q., Xu, D., Chen, H.-Y., 2018. Biosens. Bioelectron. 109, 206–213.
Karle, M., Vashist, S.K., Zengerle, R., von Stetten, F., 2016. Anal. Chim. Acta 929, 1–22.
Law, W.-C., Yong, K.-T., Baev, A., Prasad, P.N., 2011. ACS Nano 5, 4858–4864.
Lee, K.-L., Huang, J.-B., Chang, J.-W., Wu, S.-H., Wei, P.-K., 2015. Sci. Rep. 5, 8547.
Lee, K.-L., You, M.-L., Tsai, C.-H., Lin, E.-H., Hsieh, S.-Y., Ho, M.-H., Hsu, J.-C., Wei, P.-K., 2016. Biosens. Bioelectron. 75, 88–95.
Lee, K.-L., Hung, C.-Y., Pan, M.-Y., Wu, T.-Y., Yang, S.-Y., Wei, P.-K., 2018. Adv. Mater. Interf. 0, 1801064.
López-Muñoz, G.A., Estevez, M.C., Peláez-Gutierrez, E.C., Homs-Corbera, A., García-Hernandez, M.C., Imbaud, J.I., Lechuga, L.M., 2017. Biosens. Bioelectron. 96, 260–267.
Masson, J.-F., 2017. ACS Sens. 2, 16–30.
Nelson, B.P., Grimsrud, T.E., Liles, M.R., Goodman, R.M., Corn, R.M., 2001. Anal. Chem. 73, 1–7.
Olaru, A., Bala, C., Jaffrezic-Renault, N., Aboul-Enein, H.Y., 2015. Crit. Rev. Anal. Chem. 45, 97–105.
Piliarik, M., Párová, L., Homola, J., 2009. Biosens. Bioelectron. 24, 1399–1404.
Sajeesh, P., Sen, A.K., 2014. Microfluid. Nanofluidics 17, 1–52.
Schwarz, B., Reininger, P., Ristanić, D., Detz, H., Andrews, A.M., Schrenk, W., Strasser, G., 2014. Nat. Commun. 5, 4085.
Tai, Y.H., Fu, P.H., Lee, K.L., Wei, P.K., 2018. Sensors 18, 2181.
Verma, R., Gupta, B.D., 2015. Food Chem. 166, 568–575.
Wong, C.L., Olivo, M., 2014. Plasmonics 9, 809–824.
Yeung, W.K., Chen, H.Y., Sun, J.J., Hsieh, T.H., Mousavi, M.Z., Chen, H.H., Lee, K.L., Lin, H., Wei, P.K., Cheng, J.Y., 2018. Analyst 24, 4715–4722.
Zhou, W., Yang, M., Li, S., Zhu, J., 2018. Appl. Surf. Sci. 450, 328–335.